Intrinsic layer-polarized anomalous Hall effect in bilayer $MnBi_2Te_4$

Rui Peng, Ting Zhang, Zhonglin He, Qian Wu, Ying Dai,* Baibiao Huang, and Yandong Ma†
School of Physics, State Key Laboratory of Crystal Materials, Shandong University, Shandanan Street 27, Jinan 250100, China

(Received 15 September 2022; revised 7 January 2023; accepted 11 January 2023; published 10 February 2023)

Layer-polarized anomalous Hall effect (LPAHE) is an attractive phenomenon in condensed-matter physics from the standpoints of both fundamental interest and device applications. The current LPAHE research is based on the extrinsic paradigm of using external electric fields, in which the generation and control of LPAHE are not straightforward. Here, we propose a mechanism that realizes intrinsic LPAHE in bilayer lattices, through the mediation of sliding physics and Berry curvature. Moreover, this mechanism can render the LPAHE in a controllable and reversible fashion. We analyze the symmetry requirements for a system to host such intrinsic LPAHE. Its validity is further demonstrated in a real material of bilayer $MnBi_2Te_4$. By stacking with broken inversion symmetry, the layer-locked Berry curvature enables the intrinsic LPAHE in bilayer $MnBi_2Te_4$, and the switchable control of its LPAHE is achieved by sliding ferroelectricity. Our work opens a significant alternative direction for LPAHE and two-dimensional materials research.

DOI: 10.1103/PhysRevB.107.085411

I. INTRODUCTION

Hall effect is an important electronic transport phenomenon, which can lead to novel physics and efficient device applications [1–5]. There are two different microscopic mechanisms for Hall effect: one is an extrinsic process arising from scattering effects, and the other is an intrinsic mechanism related to Berry curvature [1–5]. By breaking either the inversion symmetry or time-reversal symmetry of materials, the large Berry curvature can arise because of the entangled Bloch bands with spin-orbit coupling (SOC). Two notable examples determined by this intrinsic contribution in two-dimensional (2D) materials are the valley Hall effect (VHE) [6–10] and quantum anomalous Hall effect (QAHE) [11–15]: while the former is linked to the inversion symmetry broken related valley degree of freedom [6–10], the latter connects with the time-reversal symmetry broken related spin degree of freedom [11–15]. In recent years, with the rise of 2D materials, the field of Berry curvature correlated Hall effects has undergone rapid development and received extensive attention at both the fundamental and applied levels [16–18].

Recently, as a new member of the Hall effect family, the layer-polarized anomalous Hall effect (LPAHE) is proposed in $MnBi_2Te_4$ thin films [19]. Instead of encoding with a spin or valley degree of freedom, the LPAHE rises through coupling Berry curvature to the layer degree of freedom. It is regarded as a rich playground for new physics and offers unprecedented opportunities for developing next-generation information technologies [19]. The current LPAHE research is established in the extrinsic paradigm of employing external electric fields. However, for device applications, static methods are preferred over dynamic strategies. The realization of intrinsic LPAHE is thus of significant interest, but remains elusive. Meanwhile, different from the cases of VHE and QAHE [6–15], the LPAHE is currently only realized in $MnBi_2Te_4$ thin films [19]. Actually, up to now, the LPAHE has not been thoroughly explored in monolayer or bilayer lattices. These facts pose an outstanding challenge for the field of LPAHE research.

Here, based on the paradigm of mediating sliding physics and Berry curvature, we present a mechanism for realizing LPAHE in bilayer lattices. This mechanism could enable the LPAHE to occur intrinsically, and the obtained LPAHE can be controlled and reversed through its coupling with sliding physics. The symmetry requirements for a system having such intrinsic LPAHE are mapped out. Furthermore, using first-principles calculations, we also show that such mechanism can be demonstrated in a real material of bilayer $MnBi_2Te_4$. Because of the broken inversion symmetry, the Berry curvature in bilayer $MnBi_2Te_4$ exhibits a layer-locked nature, which yields the intrinsic LPAHE. Moreover, the LPAHE in bilayer $MnBi_2Te_4$ shows a ferroelectric controllable fashion via its interlayer sliding. Our study thus not only provides a compelling mechanism toward the highly desired intrinsic LPAHE, but also extends LPAHE to the 2D lattice.

II. METHODS

First-principles calculations are performed based on density functional theory (DFT) [20] as implemented in the Vienna *ab initio* simulation package (VASP) [21]. Exchange-correlation interaction is described by the Perdew-Burke-Ernzerhof (PBE) parametrization of the generalized gradient approximation (GGA) [22]. The Mn$-d$ electrons were treated using the GGA $+ U$ approach introduced by Anisimov *et al.* [23] with the effective Hubbard $U_{\text{eff}} = 3$ eV [24]. Bi $6s$ and $6p$ states, Mn $4s$ and $3d$ states, and Te $5s$ and $5p$ states were considered to be the valence electrons. Structures are relaxed

*Corresponding author: daiy60@sdu.edu.cn
†Corresponding author: yandong.ma@sdu.edu.cn

until the force on each atom is less than 0.01 eV/Å. The cutoff energy and electronic iteration convergence criterion are set to 450 eV and 10^{-5} eV, respectively. To sample the 2D Brillouin zone, a Monkhorst-Pack (MP) k-grid mesh [25] of 9×9×1 is used. To avoid the interaction between adjacent layers, a vacuum space of 20 Å is added. The DFT-D3 (the new version density functional dispersion correction) method is employed to treat the van der Waals interaction [26]. The Berry phase approach is employed to evaluate the vertical electric polarization [27], and a ferroelectric (FE) switching pathway is obtained by the nudged elastic band (NEB) method [28]. Berry curvature and anomalous Hall conductivity are calculated using the maximally localized Wannier functions (MLWFs) as implemented in the WANNIER90 package [29]. We also employ VASPBERRY to calculate Berry curvature of the valence band [30].

III. RESULTS AND DISCUSSION

The mechanism is exemplified in a bilayer lattice. For the constituent single layers of such a bilayer lattice, two ingredients are essential. First, it should be a ferromagnetic semiconductor. Second, its band edges should have a large Berry curvature. With satisfying these two criteria, we stack them together to construct a bilayer lattice. For the bilayer lattice, two conditions are required: one is inversion/mirror symmetry breaking and the other is A-type antiferromagnetic (AFM) coupling [i.e., intralayer ferromagnetic (FM) coupling and interlayer AFM coupling].

To break the inversion symmetry, a rotation operation between the two layers is usually needed. Here, we only focus on the single layers with a C_{3z} rotation symmetry (C_{3z} symmetry), which are ubiquitous in 2D lattices. In this case, one layer needs to rotate $(2m–1)\pi/3$ (m is a nonzero integer) with respect to the other. Without losing generality, we set the rotation angle as π. To further break the mirror symmetry, an additional translation operation on one layer is required. In this regard, the top layer in the bilayer lattice can be stacked under the following symmetry operation on the bottom layer:

$$C_{2z}(0,\ 0,\ z)t(t_x,\ t_y,\ t_z).$$

Following this scenario, we obtain two high-symmetry stacking patterns of the bilayer lattice, i.e., AB′1 $[C_{2z}(0,\ 0,\ z)t(a/3,\ -a/3,\ t_z)]$ and AB′2 $[C_{2z}(0,\ 0,\ z)t(-a/3,\ a/3,\ t_z)]$; see Fig. 1. Due to the symmetry breaking, an out of plane electric polarization pointing from the bottom (top) to the top (bottom) layers is induced in the AB′1 (AB′2) configuration. Obviously, these two configurations can be regarded as two energetically equivalent FE states. Under the symmetry operations of $C_{2z}(0,\ 0,\ z)t(0,\ 0,\ t_z)$ and $C_{2z}(0,\ 0,\ z)t(a/2,\ -a/2,\ t_z)$, another two high-symmetry stacking patterns can be achieved, which are referred to as AA′ and AC′, respectively; see Fig. 1. Different from the cases of AB′1 and AB′2, the mirror and glide symmetries are preserved in AA′ and AC′, respectively. Therefore, the out of plane electric polarization has vanished in AA′ and AC′. These two configurations can be considered as the nonpolar intermediate states, which correspond to two ferroelectric transition pathways between AB′1 and AB′2, as shown in Fig. 1.

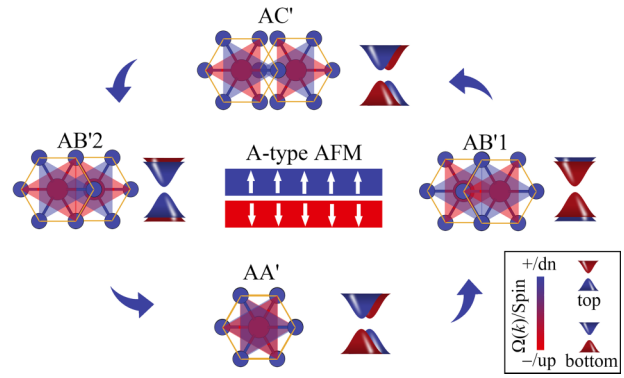

FIG. 1. Schematic diagrams of AA′, AB′1, AB′2, and AC′ configurations of a bilayer lattice and their band edges.

Different from the symmetry requirement, the latter condition is easy to be satisfied since A-type AFM coupling generally dominates the interlayer exchange interaction in bilayer systems [31,32]. Due to A-type AFM coupling, the band edges of the bilayer lattice would have layer-locked Berry curvature. As shown in Fig. 1, the Berry curvatures of band edges contributed by the top and bottom layers are opposite. In AA′ configurations, the bands are layer degenerate under the protection of Mz symmetry, while for the AB′1 configuration, arising from the existence of an out of plane electric polarization, the degeneracy of spin-up bands contributed by the bottom layer and spin-down bands contributed by the top layer is lifted. Upon shifting the Fermi level between valence (conduction) band edges contributed by the two layers, the holes (electrons) from the bottom (top) layer would feature an anomalous velocity in the presence of an in-plane electric field:

$$v \sim E \times \Omega(k).$$

As a result, the holes (electrons) would accumulate at one edge of the bottom (top) layer. Under the ferroelectric transition, the AB′1 configuration can be switched to the AB′2 configuration, wherein the holes (electrons) would accumulate at the other edge of the top (bottom) layer. This scenario is also applicable for the case where there are band inversions between two layers in bilayer systems. This successfully establishes the intrinsic LPAHE in the bilayer lattice.

After establishing the mechanism of intrinsic LPAHE in a bilayer lattice, we next discuss its realization in a real material of $MnBi_2Te_4$. Figure 2(a) presents the crystal structures of single-layer $MnBi_2Te_4$. It exhibits a trigonal lattice with the space group of $P3m1$. Therefore, it has a C_{3z} rotation symmetry. The lattice constant of single-layer $MnBi_2Te_4$ is optimized to be 4.31 Å. The valence electronic configuration of an isolated Mn atom is $3d^5\ 4s^2$. After donating two electrons to the six coordinated Te atoms, the left five electrons would half fill the Mn-d orbitals and thus result in a magnetic moment of 5 μB. Our first-principles calculations show the magnetic moment per unit cell is 5 μB, and the magnetic moment on Mn is 4.51 μB. The exchange interaction among the magnetic moments favors FM coupling. Figure 2(b) shows the band structure of single-layer $MnBi_2Te_4$ with SOC. We can see that single-layer $MnBi_2Te_4$ is a semiconductor with

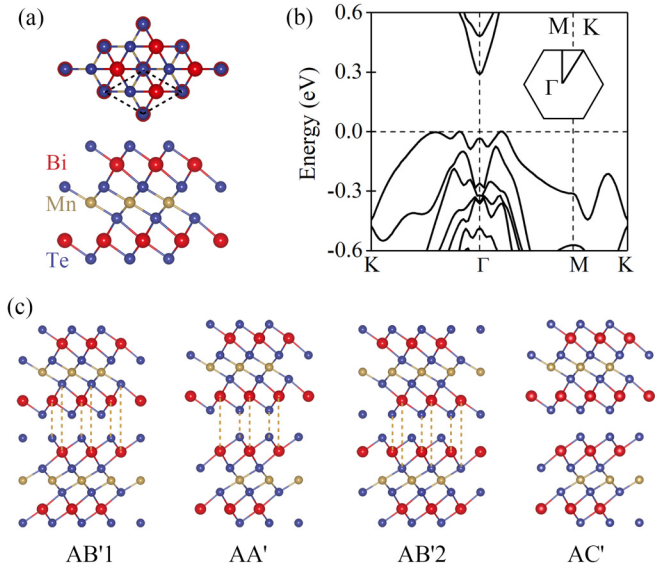

FIG. 2. (a) Crystal structures of single-layer $MnBi_2Te_4$ from top view and side view. (b) Band structures of single-layer $MnBi_2Te_4$ with SOC. The Fermi level is set to 0 eV. (c) Crystal structures of bilayer $MnBi_2Te_4$ under AB′ 1, AA′, AB′, and AC′ configurations.

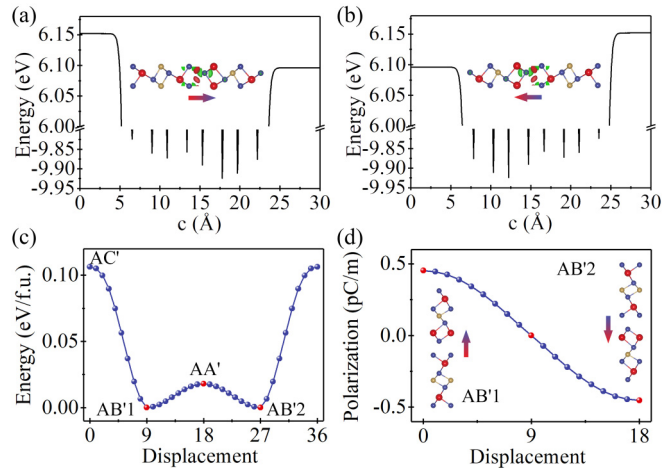

FIG. 3. Plane-averaged electrostatic potentials of (a) AB′ 1 and (b) AB′ 2 configurations for bilayer $MnBi_2Te_4$ along the c direction. Insets in (a), (b) present the corresponding charge density of AB′ 1 and AB′ 2, respectively. Red and green isosurfaces represent electron accumulation and depletion, respectively. (c) Energy profiles for FE switching of bilayer $MnBi_2Te_4$. (d) Variation of out-of-plane electric polarization of bilayer $MnBi_2Te_4$ under FE switching from AB′ 1 to AB′ 2.

an indirect band gap of 0.29 eV. The valence band minimum (CBM) is located at the Γ point, while the valence band maximum (VBM) sits along the Γ-M line. These results are consistent with previous studies [24]. Figure S1 in the Supplemental Material [33] shows the Berry curvature of single-layer $MnBi_2Te_4$. Large Berry curvature can be observed at the Γ point. Therefore, the two essential ingredients for the constituent single layers analyzed above are satisfied.

Under the operation of $C_{2z}(0,\ 0,\ z)t(t_x,\ t_y,\ t_z)$, one single-layer $MnBi_2Te_4$ is stacked on the other, forming AB′ 1, AB′ 2, AA′, and AC′ configurations; see Fig. 2(c). Among these four configurations, AB′ 1 and AB′ 2 have the lowest energy. To confirm their stabilities, the phonon spectra are calculated. As shown in Fig. S2 in the Supplemental Material [33], no imaginary frequency is found in the whole Brillouin zone for AB′ 1 and AB′ 2, indicating their dynamical stabilities, while for AA′ and AC′, there is a tiny imaginary frequency around the Γ point. To determine the magnetic ground states of these four systems, we consider A-type AFM and FM configurations; see Fig. S3 in the Supplemental Material [33]. The energy differences between A-type AFM and FM coupling are −0.57, −0.57, −0.71, and −0.02 meV for AB′ 1, AB′ 2, AA′, and AC′, respectively. This indicates that A-type AFM coupling is preferred for all these systems, satisfying the requirement for exchange interaction of the bilayer lattice. For the AB′ 1 (AB′ 2) configuration, the magnetic moment on Mn atoms of the top layer in AB′ 1 (AB′ 2) is slightly smaller than that of the bottom layer, giving rise to a net magnetic moment of 7×10^{-4} (-7×10^{-4}) μb/unit cell. We also calculate the magnetocrystalline anisotropy energy (MAE) of AB′ 1 (AB′ 2). As shown in Fig. S4 [33], the out of plane magnetization is 0.004 eV more stable than in-plane magnetization. Therefore, AB′ 1 (AB′ 2) favors out of plane magnetization. Different from these two cases, the magnetic moment on Mn atoms of the top layer cancels out that of the bottom layer in the AA′ (AC′) configuration, forming a net magnetic moment of 0 μb.

At the interface of the AB′ 1 configuration, the Te atom in the bottom layer is below the Bi atom in the top layer. This creates an out of plane electric polarization. To confirm the electric polarization, we calculate its charge density difference with respect to the two constituent single layers. As shown in Fig. 3(a), there is a redistribution for charge density in the space between the two layers; namely, the electron accumulation and depletion areas are close to the top and bottom layers, respectively, indicating the out of plane electric polarization pointing from bottom to top. This feature is also confirmed by the plane-averaged electrostatic potential of AB′ 1. As shown in Fig. 3(a), there is a positive discontinuity ($\Delta V = 0.056$ eV) between the vacuum levels of the top and bottom layers, again suggesting that the AB′ 1 configuration exhibits an out of plane electric polarization pointing upward. Using the Berry phase approach, the electric polarization is calculated to be 0.45 pC/m for the AB′ 1 configuration, which is comparable to the recently reported FE vdW multilayers [34–36]. For the AB′ 2 configuration, it is energetically equivalent to AB′ 1 and can be obtained from AB′ 1 under a mirror operation with respect to the horizontal plane. Therefore, the charge redistribution as well as ΔV are opposite to that of the AB′ 1 configuration [Fig. 3(b)]. This results in an out of plane electric polarization of −0.45 pC/m in the AB′ 2 configuration. To estimate the feasibility of FE transition between AB′ 1 and AB′ 2 configurations of bilayer $MnBi_2Te_4$, we calculate the energy barrier by using the NEB method. As discussed above, the AA′ and AC′ configurations can be considered as the nonpolar intermediate states, corresponding to two FE transition pathways between AB′ 1 and AB′ 2. As shown in Fig. 3(c), the FE switching barrier along AC′ is found to be 106 meV/f.u., while that along AA′ is only 18 meV/f.u. Therefore, the FE

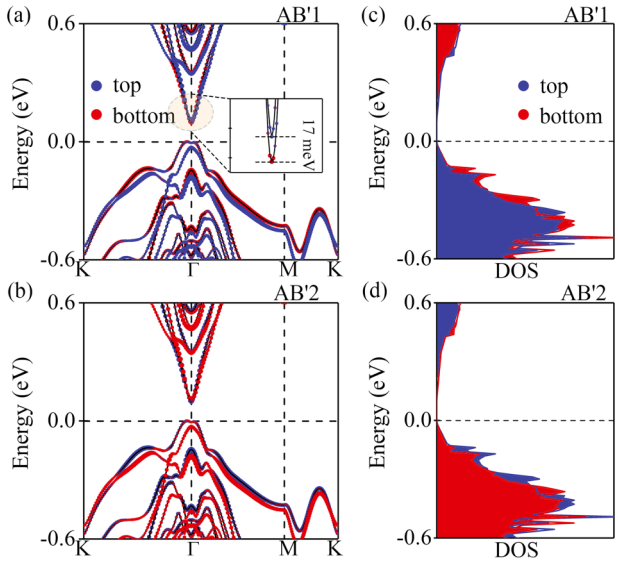

FIG. 4. (a) Band structures and (c) density of states for AB′ 1 configuration of bilayer $MnBi_2Te_4$ with SOC. (b) Band structures and (d) density of states for AB′ 2 configuration of bilayer $MnBi_2Te_4$ with SOC. The Fermi level is set to 0 eV.

transition is prone to occur along AA′, and the corresponding electric polarizations as a function of step number are shown in Fig. 3(d). It is worth emphasizing that the switching barrier is comparable to that in the recently reported FE vdW multilayers [34–36], and that in In_2Se_3 (66 meV/f.u.) [37] and $AgBiP_2Se_6$ (6.2 meV/f.u.) [38]. Therefore, the FE switching in bilayer $MnBi_2Te_4$ promises high feasibility.

Figure 4 displays the band structures and density of states of the AB′ 1 and AB′ 2 configurations. It can be seen that both systems exhibit an indirect band gap of 0.097 eV. The CBM is located at the Γ point, while the VBM sits along the K-Γ line. The bands from the top and bottom layers are separated for the AB′ 1 and AB′ 2 configurations, although both systems exhibit AFM coupling. This feature can be attributed to the existence of an out of plane electric polarization. In addition, a band inversion is observed at the Γ point. Correspondingly, for the AB′ 1 (AB′ 2) configuration, the CBM is from the bottom (top) layer, while the VBM is contributed by both layers. The separation between the bands from the top and bottom layers can also be observed from the density of states shown in Fig. 4(b). For comparison, we also calculate the band structure of AA′. As shown in Fig. S5 [33], it has an indirect band gap of 0.20 eV. Its CBM is located at the Γ point, while the VBM is along the K-Γ line. The band structure is layer degenerate along the Γ-M line due to the protection of mirror symmetry, while there are layer splittings along the K - Γ and M - K lines due to the effect of SOC and inversion symmetry breaking.

To explore the LPAHE in bilayer $MnBi_2Te_4$, we calculate the Berry curvature of the bottom conduction band in AB′ 1 using the VASPBERRY code [30]. As shown in Fig. 5(a), the Berry curvature of the bottom conduction band in AB′ 1 has large positive values around the Γ point. Accordingly, the electrons in the bottom conduction band around the Γ point for AB′ 1 would acquire an anomalous velocity $v \sim E \times \Omega(k)$, where E and $\Omega(k)$ are the external in-plane electric field and Berry curvature, respectively. When shifting the Fermi level between the CBM and the second bottom conduction band at the Γ point for AB′ 1, the electrons would be accumulated at the left edge of the bottom layer under an in-plane electric field [Fig. 5(e)], forming an anomalous Hall current, while for the AB′ 2 configuration, the Berry curvature of the bottom conduction band exhibits a large negative value around the Γ point, as shown in Fig. 5(d). By shifting the Fermi level between the CBM and the second bottom conduction band at the Γ point for AB′ 2, the electrons would be accumulated at the right edge of the top layer under an in-plane electric field [Fig. 5(e)]. This also results in an anomalous Hall current. Therefore, the long-sought LPAHE is realized in bilayer $MnBi_2Te_4$. Intriguingly, in sharp contrast to the previous work relying on an external electric field [19], the LPAHE

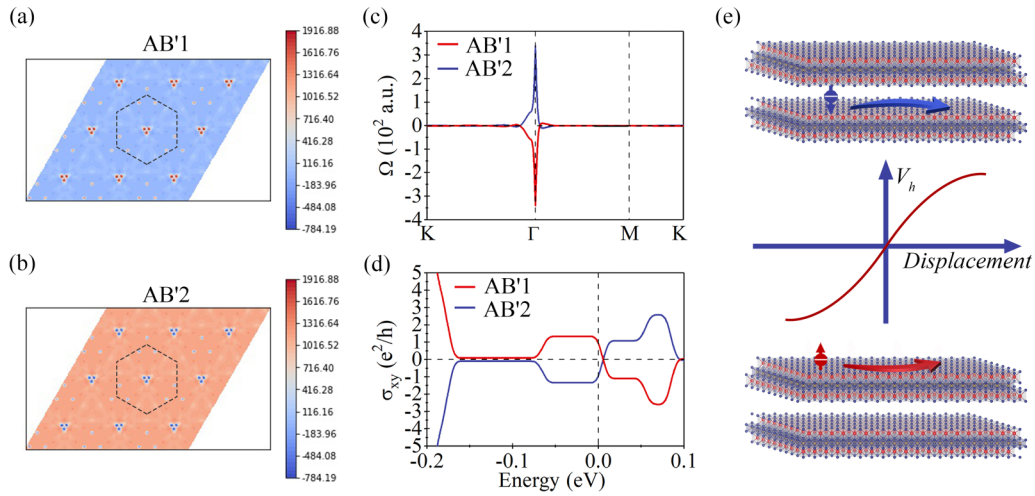

FIG. 5. Berry curvature of the bottom conduction band as a contour map in the whole Brillouin zone for (a) AB′ 1 and (b) AB′ 2 configurations of bilayer $MnBi_2Te_4$. (c) Berry curvatures along high-symmetry points for AB′ 1 and AB′ 2 configurations of bilayer $MnBi_2Te_4$. (d) Anomalous Hall conductance for AB′ 1 and AB′ 2 configurations of bilayer $MnBi_2Te_4$. (e) Schematic diagrams of intrinsic LPAHE in bilayer $MnBi_2Te_4$.

occurs spontaneously based on the intrinsic electric polarization. These two states can be easily switched to each other through ferroelectricity, as shown in Fig. 5(e), whereas in previous works on Hall effects, the reversal of the anomalous velocity of carriers is through reversing the magnetization orientation, needing large energy-dissipating electric currents [6–15].

To confirm the LPAHE in bilayer $MnBi_2Te_4$, we further investigate the anomalous Hall conductance (AHC), which is calculated using the following formula [39]:

$$\sigma = -\frac{e^2}{\hbar}\int \frac{d^2k}{(2\pi)^2}\Omega(k).$$

Here, the Berry curvature is calculated using the following formula [40]:

$$\Omega(k) = -\sum_n \sum_{n\neq n'} f_n \frac{2\mathrm{Im}\langle\psi_{nk}|v_x|\psi_{n'k}\rangle\langle\psi_{n'k}|v_y|\psi_{nk}\rangle}{(E_n - E_{n'})^2}.$$

Here, f_n is the Fermi-Dirac distribution function, ψ_{nk} is the Bloch wave function with eigenvalue E_n, and v_x (v_y) is the velocity operator along the x (y) direction. The calculated Berry curvature along the high-symmetry points and the AHC are plotted in Figs. 5(c) and 5(d), respectively. Evidently, an AHC of ~ 1 $(-1)e^2/h$ is obtained for the band around the CBM of AB′ 1 (AB′ 2). This firmly confirms the LPAHE in bilayer $MnBi_2Te_4$.

IV. CONCLUSION

In summary, a unique mechanism for intrinsic LPAHE in bilayer lattices is proposed based on the paradigm of mediating sliding physics and Berry curvature. Through coupling with sliding physics, the proposed LPAHE can be controlled and reversed via ferroelectricity. The symmetry requirements for hosting such intrinsic LPAHE are mapped out. Using first-principles calculations, this mechanism is further demonstrated in a real material of bilayer $MnBi_2Te_4$. The Berry curvature in bilayer $MnBi_2Te_4$ displays a layer-locked nature, resulting in the LPAHE intrinsically, and the LPAHE in bilayer $MnBi_2Te_4$ is ferroelectric controllable via interlayer sliding. The proposed mechanism and the candidate bilayer $MnBi_2Te_4$ thus have the possibility of impacting LPAHE research in 2D lattices.

ACKNOWLEDGMENTS

This work is supported by the National Natural Science Foundation of China (Grants No. 12274261 and No. 12074217), Shandong Provincial Natural Science Foundation (Grants No. ZR2019QA011 and No. ZR2019MEM013), Shandong Provincial Key Research and Development Program (Major Scientific and Technological Innovation Project) (Grant No. 2019JZZY010302), Shandong Provincial Key Research and Development Program (Grant No. 2019RKE27004), Shandong Provincial QingChuang Technology Support Plan (Grant No. 2021KJ002), Qilu Young Scholar Program of Shandong University, and Taishan Scholar Program of Shandong Province.

[1] N. Nagaosa, J. Sinova, S. Onoda, A. H. MacDonald, and N. P. Ong, Anomalous Hall effect, Rev. Mod. Phys. **82**, 1539 (2010).
[2] Z. Fang, N. Nagaosa, K. S. Takahashi, A. Asamitsu, R. Mathieu, T. Ogasawara, H. Yamada, M. Kawasaki, Y. Tokura, and K. Terakura, The anomalous Hall effect and magnetic monopoles in momentum space, Science **302**, 92 (2003).
[3] F. D. M. Haldane, Berry Curvature on the Fermi Surface: Anomalous Hall Effect as a Topological Fermi-Liquid Property, Phys. Rev. Lett. **93**, 206602 (2004).
[4] D. Xiao, M. C. Chang, and Q. Niu, Berry phase effects on electronic properties, Rev. Mod. Phys. **82**, 1959 (2010).
[5] S. Nakatsuji, N. Kiyohara, and T. Higo, Large anomalous Hall effect in a non-collinear antiferromagnet at room temperature, Nature (London) **527**, 212 (2015).
[6] R. Peng, Y. Ma, X. Xu, Z. He, B. Huang, and Y. Dai, Intrinsic anomalous valley Hall effect in single-layer Nb_3I_8, Phys. Rev. B **102**, 035412 (2020).
[7] R. Peng, Z. He, Q. Wu, Y. Dai, B. Huang, and Y. Ma, Spontaneous valley polarization in 2D organometallic lattice, Phys. Rev. B **104**, 174411 (2021).
[8] Z. He, R. Peng, X. Feng, X. Xu, Y. Dai, B. Huang, and Y. Ma, Two-dimensional valleytronic semiconductor with spontaneous spin and valley polarization in single-layer Cr_2Se_3, Phys. Rev. B **104**, 075105 (2021).
[9] W.-Y. Tong, S.-J. Gong, X. Wan, and C.-G. Duan, Concepts of ferrovalley material and anomalous valley Hall effect, Nat. Commun. **7**, 13612 (2016).
[10] H. Hu, W. Tong, Y. Shen, X. Wan, and C. Duan, Concepts of the half-valley-metal and quantum anomalous valley Hall effect, npj Comput. Mater. **6**, 129 (2020).
[11] F. D. M. Haldane, Model for a Quantum Hall Effect without Landau Levels: Condensed-Matter Realization of the "Parity Anomaly", Phys. Rev. Lett. **61**, 2015 (1988).
[12] K. He, Y. Wang, and Q. K. Xue, Quantum anomalous Hall effect, Nat. Sci. Rev. **1**, 38 (2014).
[13] Z. Liu, G. Zhao, B. Liu, Z. Wang, J. Yang, and F. Liu, Intrinsic Quantum Anomalous Hall Effect with In-Plane Magnetization: Searching Rule and Material Prediction, Phys. Rev. Lett. **121**, 246401 (2018).
[14] Z. He, R. Peng, Y. Dai, B. Huang, and Y. Ma, Single-layer ScI_2: A Paradigm for Valley-Related Multiple Hall Effect, Appl. Phys. Lett. **119**, 243102 (2021).
[15] Y. Jin, Z. Chen, B. Xia, Y. Zhao, R. Wang, and H. Xu, Large-gap quantum anomalous Hall phase in hexagonal organometallic frameworks, Phys. Rev. B **98**, 245127 (2018).
[16] L. Smejkal, R. Gonzalez-Hernandez, T. Jungwirth, and J. Sinova, Crystal Hall effect in collinear antiferromagnets, Sci. Adv. **6**, eaaz8809 (2020).

[17] N. J. Ghimire, A. S. Botana, J. S. Jiang, J. Zhang, Y.-S. Chen, and J. F. Mitchell, Large anomalous Hall effect in the chiral-lattice antiferromagnet $CoNb_3S_6$, Nat. Commun. **9**, 3280 (2018).

[18] D. Shao, J. Ding, G. Gurung, S. Zhang, and E. Y. Tsymbal, Interfacial Crystal Hall Effect Reversible by Ferroelectric Polarization, Phys. Rev. Appl. **15**, 024057 (2021).

[19] A. Gao, Y.-F. Liu, C. Hu, J.-X. Qiu, C. Tzschaschel, B. Ghosh, S.-C. Ho, D. Bérubé, R. Chen, H. Sun *et al.*, Layer Hall effect in a 2D topological axion antiferromagnet, Nature (London) **595**, 521 (2021).

[20] W. Kohn and L. J. Sham, Self-consistent equations including exchange and correlation effects, Phys. Rev. **140**, A1133 (1965).

[21] G. Kresse and J. Furthmüller, Efficient iterative schemes for *ab initio* total-energy calculations using a plane-wave basis set, Phys. Rev. B **54**, 11169 (1996).

[22] J. P. Perdew, K. Burke, and M. Ernzerhof, Generalized Gradient Approximation Made Simple, Phys. Rev. Lett. **77**, 3865 (1996).

[23] V. I. Anisimov, J. Zaanen, and O. K. Andersen, Band theory and Mott insulators: Hubbard *U* instead of Stoner *I*, Phys. Rev. B **44**, 943 (1991).

[24] M. M. Otrokov, I. P. Rusinov, M. Blanco-Rey, M. Hoffmann, A. Yu. Vyazovskaya, S. V. Eremeev, A. Ernst, P. M. Echenique, A. Arnau, and E. V. Chulkov, Unique Thickness-Dependent Properties of the van der Waals Interlayer Antiferromagnet $MnBi_2Te_4$ Films, Phys. Rev. Lett. **122**, 107202 (2019).

[25] H. J. Monkhorst and J. D. Pack, Special points for Brillouin-zone integrations, Phys. Rev. B **13**, 5188 (1976).

[26] S. Grimme, J. Antony, S. Ehrlich, and H. Krieg, A consistent and accurate *ab initio* parametrization of density functional dispersion correction (DFT-D) for the 94 elements H-Pu, J. Chem. Phys. **132**, 154104 (2010).

[27] R. D. King-Smith and D. Vanderbilt, Theory of polarization of crystalline solids, Phys. Rev. B **47**, 1651 (1993).

[28] G. Mills, H. Jónsson, and G. K. Schenter, Reversible work transition state theory: Application to dissociative adsorption of hydrogen, Surf. Sci. **324**, 305 (1995).

[29] A. A. Mostofi, J. R. Yates, G. Pizzi, Y.-S. Lee, I. Souza, D. Vanderbilt, and N. Marzari, An updated version of WANNIER90: A tool for obtaining maximally-localised Wannier functions, Comput. Phys. Commun. **185**, 2309 (2014).

[30] H. Kim, C. Li, J. Feng, J. Cho, and Z. Zhang, Competing magnetic orderings and tunable topological states in two-dimensional hexagonal organometallic lattices, Phys. Rev. B **93**, 041404(R) (2016).

[31] S. Gong, C. Gong, Y. Sun, W. Tong, C. Duan, J. Chua, and X. Zhang, Electrically induced 2D half-metallic antiferromagnets and spin field effect transistors, Proc. Natl. Acad. Sci. USA **115**, 8511 (2018).

[32] H. Lv, Y. Niu, X. Wu, and J. Yang, Electric-field tunable magnetism in van der Waals bilayers with A-type antiferromagnetic order: Unipolar versus bipolar magnetic semiconductor, Nano Lett. **21**, 7050 (2021).

[33] See Supplemental Material at http://link.aps.org/supplemental/10.1103/PhysRevB.107.085411 for stability and electronic properties of bilayer $MnBi_2Te_4$.

[34] T. Zhang, Y. Liang, X. Xu, B. Huang, Y. Dai, and Y. Ma, Ferroelastic-ferroelectric multiferroics in a bilayer lattice, Phys. Rev. B **103**, 165420 (2021).

[35] Y. Liang, S. Shen, B. Huang, Y. Dai, and Y. Ma, Intercorrelated ferroelectrics in 2D van der Waals materials, Mater. Horiz. **8**, 1683 (2021).

[36] Q. Yang, M. Wu, and J. Li, Origin of two-dimensional vertical ferroelectricity in WTe_2 bilayer and multilayer, J. Phys. Chem. Lett. **9**, 7160 (2018).

[37] W. Ding, J. Zhu, Z. Wang, Y. Gao, D. Xiao, Y. Gu, Z. Zhang, and W. Zhu, Prediction of intrinsic two-dimensional ferroelectrics in In_2Se_3 and other III_2-VI_3 van der Waals materials, Nat. Commun. **8**, 14956 (2017).

[38] B. Xu, H. Xiang, Y. Xia, K. Jiang, X. Wan, J. He, J. Yin, and Z. Liu, Monolayer $AgBiP_2Se_6$: An atomically thin ferroelectric semiconductor with out-plane polarization, Nanoscale **9**, 8427 (2017).

[39] Y. G. Yao, L. Kleinman, A. H. MacDonald, J. Sinova, T. Jungwirth, D.-S. Wang, E. Wang, and Q. Niu, First Principles Calculation of Anomalous Hall Conductivity in Ferromagnetic bcc Fe, Phys. Rev. Lett. **92**, 037204 (2004).

[40] D. J. Thouless, M. Kohmoto, M. P. Nightingale, and M. den Nijs, Quantized Hall Conductance in a Two-Dimensional Periodic Potential, Phys. Rev. Lett. **49**, 405 (1982).